Corrosion Science 176 (2020) 109015

Contents lists available at ScienceDirect

Corrosion Science

journal homepage: www.elsevier.com/locate/corsci

The contribution of Cr and Mo to the passivation of Ni22Cr and Ni22Cr10Mo alloys in sulfuric acid

Xuejie Li [a,1], Jeffrey D. Henderson [b,1], Fraser P. Filice [b], Dmitrij Zagidulin [b], Mark C. Biesinger [b,c], Fan Sun [a], Bingnan Qian [a], David W. Shoesmith [b,c], James J. Noël [b,c,*], Kevin Ogle [a,**]

[a] Chimie-ParisTech, PSL University, IRCP-CNRS, 75005, Paris, France
[b] Department of Chemistry, Western University, London, ON, N6A 5B7, Canada
[c] Surface Science Western, Western University, London, ON, N6G 0J3, Canada

ARTICLE INFO

Keywords:
Passivation
Ni alloys
Mo
Kinetics
Alloys

ABSTRACT

The beneficial effects of Mo on passive film formation were investigated for Ni22Cr10Mo with AESEC and XPS by comparison with Ni22Cr and pure Ni and Mo. Both spontaneous ($E \approx -0.2\ V_{SCE}$) and anodic passivation ($E = 0.3\ V_{SCE}$) showed Cr surface accumulation, while significant Mo accumulation (as Mo(IV)) only occurred during spontaneous passivation with a markedly reduced open circuit corrosion rate as a consequence. Mo facilitated the active to passive transition in the low potential domain probably by favoring the oxidation of Cr to Cr_2O_3 over $Cr(OH)_3$. At higher potential, Mo dissolved as Mo(VI) and did not accumulate in the film.

1. Introduction

Ni-Cr-Mo alloys are a class of corrosion resistant alloys commonly used in the petrochemical, nuclear, and chemical processing industries and have been suggested as one of the corrosion resistant engineering barriers in the proposed Yucca Mountain spent nuclear fuel repository [1]. The alloying elements, Cr and Mo, play an important role in establishing the corrosion resistance of the alloy. Cr is known to promote the formation of a corrosion resistant surface oxide, known also as a passive film. That Cr is the majority species in the passive film has been confirmed by various techniques [2–4]. Additions of Mo to the alloy have been shown to stabilize the passive film, especially when there is a risk of localized corrosion [5–7]. The benefits of alloyed Mo are empirically known, yet the underlying mechanisms are not well understood [8]. Many studies have been carried out to clarify the role of Mo and yet even the conditions under which Mo may be accumulate in the passive film remain uncertain. Some studies suggest Mo enriches in the film [9–11] while some others suggest the opposite [12–15]. The proposed mechanisms by which Mo may promote passivation include a beneficial influence on repassivation, in which case Mo may have only a transitory existence in the film [7,16,17], and/or the formation of an ion-selective layer of Mo species, reinforcing the protectiveness of the Cr-based film [18,19].

Zhang et al. [20] recently proposed a theory that the enrichment or depletion of Mo in the passive film is strongly correlated with the nature of the solution, based on their aberration-corrected transmission electron microscopy results. Solutions containing Cl^- induced the enrichment of Mo. They proposed that Cl^- ions could extract Mo from the matrix into the electrolyte solution by forming a soluble $MoCl_x$ complex, then the $MoCl_x$ could be further oxidized to Mo oxide and enriched in the outer region of the passive film. However, other researchers have reported Mo depletion in the passive film in solutions containing Cl^- [13, 21]. Inline ICP-MS, coupled with other *in situ* and *ex situ* techniques, was recently employed by Cwalina et al. [22] to investigate the kinetics of oxide formation and growth on Ni22Cr and Ni22Cr6Mo (wt.%) alloys in 0.1 M NaCl solutions with the pH adjusted to 4 and 10. It was found that the addition of Mo to the Ni22Cr alloy resulted in the increased enrichment of Cr in the surface film.

We have recently demonstrated that the accumulation of Cr and Mo could be monitored quantitatively as a function of time during electrochemical experiments with a commercial Ni22Cr13Mo alloy, Hastelloy C-22, in sulfuric acid, using atomic emission spectroelectrochemistry (AESEC) [23]. Besides having the ability to passivate in sulfuric acid when an anodic polarization was applied, it also spontaneously

* Corresponding author at: Department of Chemistry, Western University, London, ON, N6A 5B7, Canada.
** Corresponding author.
E-mail addresses: jjnoel@uwo.ca (J.J. Noël), kevin.ogle@chimieparistech.psl.eu (K. Ogle).
[1] Indicates equal contribution.

https://doi.org/10.1016/j.corsci.2020.109015
Received 31 July 2020; Received in revised form 16 September 2020; Accepted 19 September 2020
Available online 24 September 2020
0010-938X/

passivated at the open-circuit (or corrosion) potential, E_{oc}. We demonstrated that the accumulation of surface Cr occurred during both spontaneous passivation and anodic passivation, attributed to the build-up of Cr oxides as a passive film. The film was removed by a subsequent cathodic activation. By contrast, Mo accumulation only occurred during spontaneous passivation at open circuit following cathodic activation. This excess Mo partially dissolved during a subsequent anodic passivation step ($E = 0.3\ V_{SCE}$) and almost completely dissolved during the following cathodic activation ($E = -0.8\ V_{SCE}$). Therefore, it was proposed that Mo accumulation in the oxide film was strongly influenced by the history of the material and the specific conditions of passivation. Based on thermodynamic considerations, the accumulation of Mo in the film during spontaneous passivation at lower potential was attributed to the formation of insoluble Mo(IV) oxides; their subsequent dissolution at higher potential was attributed to the oxidation of these oxides to the more soluble Mo(VI) species.

The goal of this work is to further clarify the role of Mo on the kinetics of passive film formation and dissolution. To this end we present new results with a simplified ternary alloy (Ni22Cr10Mo). To highlight the role of Mo, we compare the behavior of this material with the binary alloy (Ni22Cr) and with pure Mo and Ni using a combination of *in situ* AESEC and *ex situ* XPS for the alloys.

2. Experimental

2.1. Sample preparation

The Ni22Cr and Ni22Cr10Mo (wt.%) alloy ingots were fabricated using an Edmund Bühler MIM1 arc-melting system operated under an Ar atmosphere. Pure Ni (99.99 %), Cr (99.99 %), and Mo (99.99 %) metals were used to obtain the desired compositions. The melting process was repeated at least three times for each alloy, with ingots turned over after each melting process. The as-fabricated ingots were annealed at 1000 °C for 24 h under vacuum (10^{-5} mbar). The annealed ingots were then cold-rolled into sheets. The as-rolled sheets were solution-treated at 1000 °C under vacuum (10^{-5} mbar) for 24 h and then quenched in water. The as-quenched samples were confirmed to be single fcc phase using X-ray diffraction (XRD), not shown. Samples used for AESEC and XPS experiments were cut from the sheet, mechanically ground by a series of SiC papers up to P4000 then polished to a mirror finish using 1 μm diamond suspension. Before each experiment, samples were rinsed with deionized (DI) water.

2.2. Atomic emission spectroelectrochemistry

Atomic emission spectroelectrochemistry (AESEC) is based on the combination of an electrochemistry flow cell with an inductively coupled plasma atomic emission spectrometer (ICP-AES). The AESEC technique has been comprehensively reviewed in the recently published article by Ogle [24]. The principle of AESEC is to collect and analyze species released from a sample surface in real-time while conducting electrochemical measurements. To achieve this, a specially designed flow cell is used to carry out the electrochemistry. Meanwhile, the ICP-AES is used to detect the dissolved species downstream. As a result, the dissolution rate of each element as a function of time can be obtained. Additionally, by assuming the oxidation state of each element, the dissolution rates can be converted into elemental currents to compare with the external electrical current measured by the potentiostat. The emission wavelengths selected for analysis of Ni, Cr, and Mo are shown in Table 1, as well as the detection limits defined as ($C_{3\sigma} = 3\sigma/\kappa$) where σ is the standard deviation of background intensity in the absence of the element and κ is the sensitivity (i.e. slope) of the intensity vs. concentration curve. Note that detection limits may vary considerably from one experiment to the next depending on plasma conditions. In all cases, the polychromator of the ICP-AES spectrometer was used for both Ni and Cr, and the monochromator was used for Mo.

Table 1
Wavelengths and typical experimental detection limits for Ni and Cr (polychromator), and Mo (monochromator). Equivalent dissolution rates and current densities at the flow rate of 1.5 mL/min are also shown, the latter were calculated with the oxidation states of Ni(II), Cr(III), and Mo(VI).

Element	Ni	Cr	Mo
Wavelength / nm	231.604	267.716	202.032
Detection limit / ng cm^{-3}	12	6.2	1.4
ν_M / ng cm^{-2} s^{-1}	0.30	0.16	0.035
j_M / μA cm^{-2}	0.99	0.89	0.21

Additionally, the equivalent detection limits expressed in dissolution rates and electrical current densities are shown. The calculation of ν_M and j_M are described in the data treatment section.

2.3. Electrochemical setup

Immediately after surface preparation, samples were assembled with the homemade electrochemical flow cell, exposing either 0.5 or 1 cm^2 of the surface to the electrolyte. A typical three electrode system was used during all electrochemical measurements. Electrochemical experiments were performed using a Gamry Instruments Reference 600 for AESEC experiments or a Solartron 1287 potentiostat for XPS sample preparation. The sample served as the working electrode (WE). A Pt foil serving as the counter electrode (CE) and a saturated calomel electrode (SCE) as the reference electrode (RE) were placed in a second compartment separated from the WE by a conductive membrane. Solutions of 2 M H_2SO_4 were made by mixing DI water and 95 % H_2SO_4. The electrolyte was pumped into the cell at a speed of ~3 mL per minute (cyclic potentiostatic experiments) or ~1.5 mL per minute (potentiodynamic polarization). Deaeration was achieved by sparging Ar gas into the solution for 30 min. before the experiment and continuously until the experiment finished. Aerated solution refers to the solution exposed to air.

2.4. Data treatment

The emission intensity of the element M at the specific wavelength (I_λ) obtained from ICP-AES (Horiba, Ultima 2C) was converted into a dissolution rate (ν_M) according to Eq. (1).

$$\nu_M = f\ (I_\lambda - I_\lambda^\circ)/\kappa_\lambda A \quad (1)$$

where I_λ° is the background intensity, and κ_λ is the sensitivity factor of element M at the chosen wavelength, determined by conventional ICP-AES calibration methods using commercially available element standards (PlasmaCAL, SCP Science). The flow rate, f, was measured to a relative error of ≤ 1% for each experiment. The surface area, A, is the geometric surface of the WE exposed to the electrolyte, defined by the O-ring of the electrochemical flow cell.

The dissolution rate of element M (ν_M) may be normalized to the bulk composition relative to a chosen element (N) by Eq. (2).

$$\nu_M^{\cdot} = \left(\frac{X_N}{X_M}\right) \nu_M \quad (2)$$

where X_M and X_N are the mass fractions of elements M and N, respectively.

The accumulated surface excess (relative to Ni) of an element M, Θ_M, from time A to time B, may be determined by Eq. (3)

$$\Theta_M = \int_A^B \left(\frac{X_M}{X_{Ni}}\nu_{Ni} - \nu_M\right) \quad (3)$$

An increase of Θ_M indicates M is accumulating on the surface while a decrease of Θ_M indicates excess dissolution of M.

To compare the elemental dissolution rate (ν_M) with the external

electrical current density (j_e) measured by the potentiostat, ν_M may be transformed to an equivalent elemental current density, j_M, by Eq. (4):

$$j_M = (n_M F \nu_M)/m_M \quad (4)$$

where n is the presumed number of electron(s) involved in the electrochemical dissolution reaction, m_M is the atomic mass of M, and F is the Faraday constant.

During transient experiments at short times, the comparison of j_e with the sum of the elemental currents (Σj_M) requires a correction of the residence time distribution, h(t), of dissolved elements in the flow cell and capillaries of the system [25]. It has been demonstrated that h(t) follows a log-normal function:

$$h(t) = \begin{cases} \sqrt{\frac{\beta}{\pi\tau^2}} \cdot e^{-\frac{1}{4\beta}} \cdot e^{-\beta\left(\ln\frac{t}{\tau}\right)^2} & if\ t > 0 \\ 0\ if\ t = 0 \end{cases} \quad (5)$$

where the values of τ and β are empirically determined parameters, 0.99 and 10.23 respectively, obtained by applying a short anodic pulse to Cu in HCl solution [25,26]. It was demonstrated that the correction of the current density may be realized by convoluting j_e using Eq. (6) [26].

$$j_e^*(t) = \int_0^t j_e(\tau) h(t-\tau) d\tau \quad (6)$$

2.5. XPS characterization

Specimens considered for XPS characterization were prepared using the identical electrochemical flow cell setup enclosed in a N_2-filled glove box to minimize the influence of oxygen exposure. The oxygen level in the glovebox was controlled in the range of 50 ppm–100 ppm. After treatment, each sample was rinsed with DI water, dried, and stored in a separate Ar-filled glove box with oxygen levels continuously maintained at 0.1 ppm until XPS analysis.

XPS measurements were carried out using a Kratos AXIS Supra spectrometer. All spectra were collected using the monochromatic Al Kα X-ray source (photon energy =1486.6 eV) operating at 12 mA and 15 kV (180 W). During analysis, pressures inside the analysis chamber were maintained at, or below, 10^{-8} Torr. Calibration of the instrument work function was done using the binding energy (B.E.) of a standard metallic Au sample ($4f_{7/2}$ at 83.95 eV). In all spectra, photoelectrons were collected from an area of 700 µm x 400 µm. For all samples, spectra were collected at multiple take-off angles including 90, 50, 30, and 15°; however, only the 90° data set is described here due to the high noise level associated with the lower angles.

Survey spectra were recorded over a B.E. of 0–1200 eV using a pass energy of 160 eV at a step size of 1 eV. High-resolution spectra of the C 1s, O 1s, Ni 2p, Cr 2p, Mo 3d, and S 2p lines were collected using a pass energy of 20 eV at a step size of 0.1 eV. All spectra were charge-corrected by setting the aliphatic (C-C) adventitious carbon signal to 284.8 eV. All signal processing and deconvolution were performed with CasaXPS software (v2.3.19) using a Shirley background subtraction. The deconvolution of high-resolution spectra was done using previously determined fitting parameters and constraints collected from standard metallic and oxide samples of Ni [27,28], Cr [27,29], and Mo [30].

3. Results

3.1. Overview of electrochemical behavior

Fig. 1 shows conventional polarization curves for Ni22Cr and Ni22Cr10Mo alloys in aerated and deaerated 2 M H_2SO_4. Both alloys showed an anodic peak denoting the active to passive transition and a well-defined passive domain. For convenience, these two anodic domains will be labelled A1 (~ -0.25 V_{SCE} < E < ~ 0.1 V_{SCE}) and A2 (E > ~ 0.1 V_{SCE}) respectively as indicated. For Ni22Cr10Mo, current densities were lower in magnitude in both the cathodic domain (C, E < -0.25 V_{SCE}) and the active to passive transition (A1) as compared to Ni22Cr. The effect was particularly marked for the critical current (maximum of A1) for which approximately an order of magnitude decrease was observed. Within the passive domain (A2), current densities were comparable for both Ni22Cr and Ni22Cr10Mo. By comparing the potentiodynamic polarization curves, we conclude that Mo promotes the formation of the passive film during the active to passive transition in the low potential domain (A1) but does not seem to alter the protective nature of the film once formed in the high potential domain (A2). This is consistent with what has been previously reported on Ni alloys [19,31,32] and for stainless steel [33].

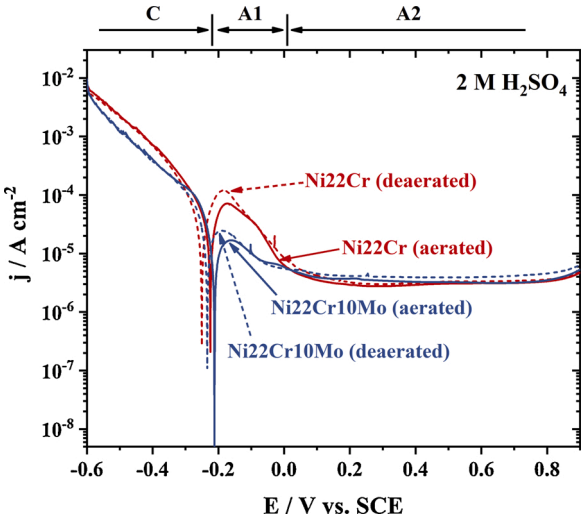

Fig. 1. The potentiodynamic polarization curves of Ni22Cr (red) and Ni22Cr10Mo (blue) alloys in aerated (solid line) and deaerated (dotted lines) 2 M H_2SO_4, at ambient temperature, from -0.6 V_{SCE} to 0.9 V_{SCE} at 0.5 mV s^{-1} (For interpretation of the references to colour in this figure legend, the reader is referred to the web version of this article.).

Deaeration of the electrolyte had little influence on the electrochemistry (Fig. 1) for either alloy. The slight increase in the critical current density after deaeration may be attributed to the elimination of oxygen reduction, which also occurs in this potential range, the total current being the sum of the cathodic and anodic partial reactions. This same effect also accounts for the slight shift of the peak position and E_{corr} to a lower potential in both cases. Although the effect was minimal, deaeration was important for this study so as to have the maximum resolution of the anodic reactions in the domain A1, where the effect of Mo is most clearly visible.

3.2. Elemental electrochemistry of Ni22Cr and Ni22Cr10Mo

Elementally resolved polarization curves in aerated and deaerated 2 M H_2SO_4 solutions are shown in Figs. 2 and 3 for alloys Ni22Cr and Ni22Cr10Mo, respectively. The conventional polarization curve, identical to Fig. 1, is shown in the upper part of each figure. The lower part shows the elemental currents for Ni (j_{Ni}), Cr (j_{Cr}), and Mo (j_{Mo}). Elemental currents were calculated from the elemental dissolution rate according to Eq. (4) assuming $n_{Ni} = 2$, $n_{Cr} = 3$ and $n_{Mo} = 6$. The green dashed lines overlaid with j_{Cr} and j_{Mo} are the expected elemental currents, j'_{Cr} and j'_{Mo}, assuming congruent dissolution with Ni, based on the following equation:

$$j'_M = \left(\frac{\chi_M}{\chi_{Ni}} \frac{n_M}{n_{Ni}}\right) j_{Ni} \quad (7)$$

where χ_M is the mole ratio of element M (Cr or Mo). The sum of the

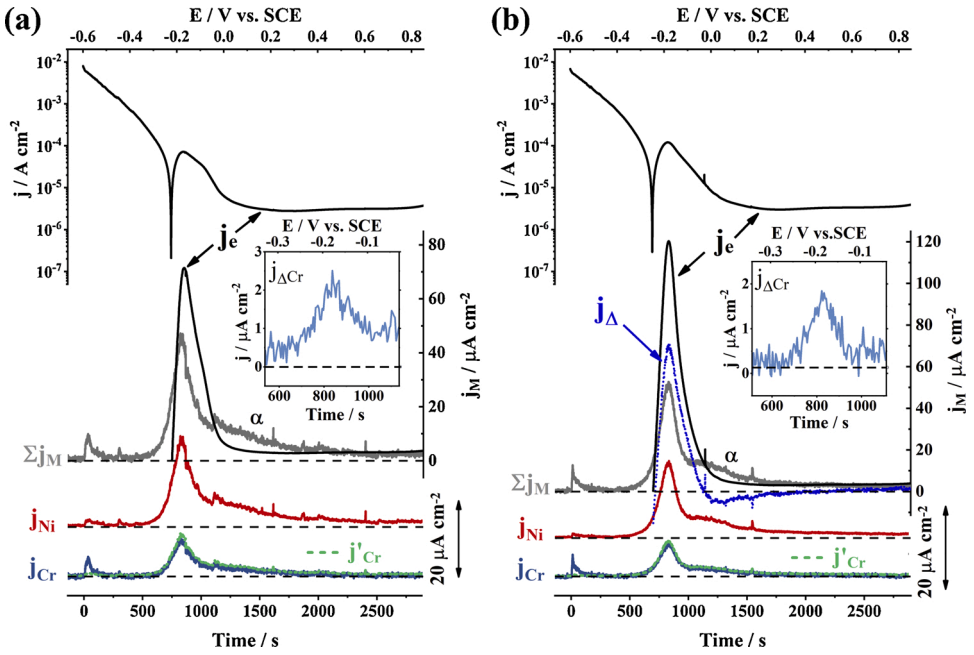

Fig. 2. Elemental resolved potentiodynamic polarization curve for Ni22Cr recorded in aerated (a) and deaerated (b) 2 M H_2SO_4. For j_e in the bottom panels, only positive values are shown. Σj_M indicates the sum of the elemental currents. Elemental currents of Ni(II) and Cr(III) are offset for clarity. The green dashed lines are assumed congruent elemental currents for Cr (relative to Ni). Shown in insets are $j_{\Delta Cr}=j'_{Cr} - j_{Cr}$, showing the accumulation of Cr during the active to passive transition (For interpretation of the references to colour in this figure legend, the reader is referred to the web version of this article.).

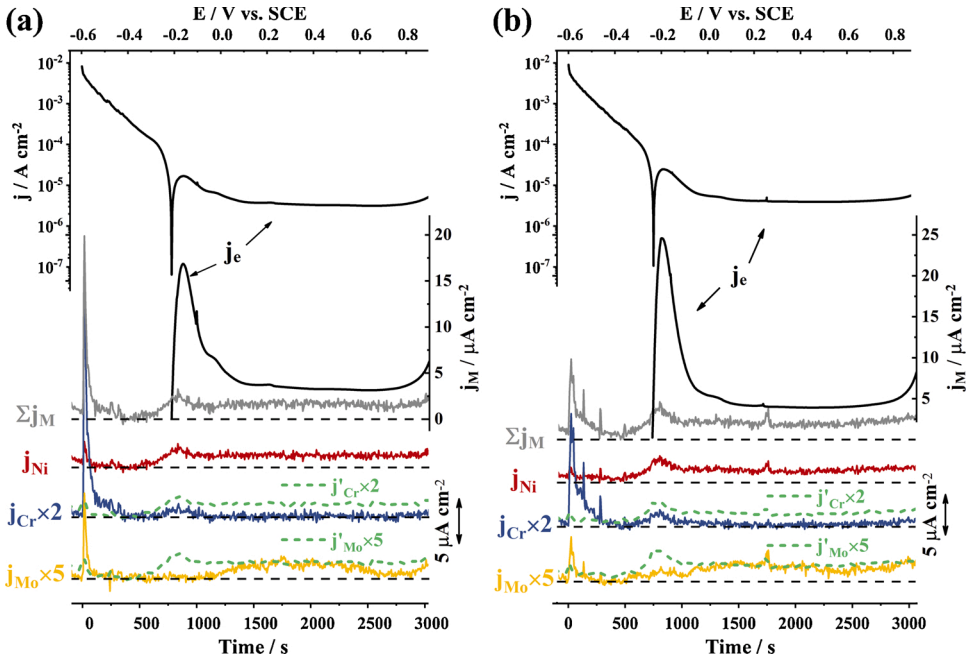

Fig. 3. Elemental resolved potentiodynamic polarization curve for Ni22Cr10Mo in aerated (a) and deaerated (b) 2 M H_2SO_4. For j_e in the bottom panels, only positive values are shown. Σj_M indicates the sum of the elemental currents. Elemental currents of Ni(II), Cr(III), and Mo(VI) are offset for clarity. The green dashed lines are the assumed congruent elemental currents for Cr and Mo (For interpretation of the references to colour in this figure legend, the reader is referred to the web version of this article.).

elemental dissolution currents, Σj_M, is also compared with the total electrical current, j_e.

During all polarization measurements in Figs. 2 and 3, an excess dissolution of Cr ($j_{Cr} >> j'_{Cr}$) was seen at the onset of the cathodic polarization (-0.6 V_{SCE}). For Ni22Cr10Mo, excess Mo dissolution ($j_{Mo} >> j'_{Mo}$) was also observed. This may be attributed to the dissolution of the air-formed oxide. As the applied potential was increased, elemental currents stabilized at low values, around the detection limit. This continued until the active to passive transition, where both j_{Ni} and j_{Cr} showed a peak. Deaeration had little to no effect on the elemental dissolution rates.

Unlike the case for a 304 stainless steel [34], anodic dissolution of Ni22Cr was not faradaic. Considering the active peak for the deaerated solution, a faradaic dissolution yield of 56.7 % was obtained based on the assumption of $n_{Ni} = 2$ and $n_{Cr} = 3$. The electrical current that did not lead to dissolution ($j_\Delta = j_e - \Sigma j_M$, shown as the blue dotted line in Fig. 2b) may be attributed to the formation of insoluble oxides for the deaerated solution, as the cathodic current is negligible. Integration of j_Δ yielded 14 mC cm^{-2} corresponding to a film thickness of 7 nm if only the formation of Cr_2O_3 is considered.

The accumulation of Cr in the film was observed in the active to passive transition domain (A1) for the Ni22Cr alloy. This is indicated by calculating the partial rate of Cr accumulation, $j_{\Delta Cr} = j'_{Cr} - j_{Cr}$, shown in the insets of Fig. 2a and b. A broad, secondary dissolution peak (labelled "α") was detected during the descending edge of the active dissolution peak, ($\Sigma j_M > j_e$) implying that non-faradaic dissolution occurred. This supports the idea that excess oxide formation occurred in the active domain, and this excess oxide subsequently dissolved to leave the final

passive film. Lutton et al. also observed a delayed dissolution of excess oxide during potentiostatic passivation experiments on Ni22Cr and Ni22Cr6Mo alloys [35].

For Ni22Cr10Mo (Fig. 3), $j_e > \Sigma j_M$ in the active to passive transition domain (A1) and the passive domain (A2), indicating the formation of insoluble species. However, the contributions of Cr and Mo changed markedly with potential. During the active to passive transition, a significant Mo accumulation ($j_{Ni} >> j_{Mo} \approx 0$) and a less significant Cr accumulation were observed. In the passive domain, Mo dissolution approached a congruent level and Cr dissolution was below the detection limit.

3.3 Electrochemistry of pure Mo and Ni

To further clarify the behavior of Mo as a function of potential, the polarization curve of nominally pure Mo was obtained, Fig. 4. Also shown for comparison is a similar curve for nominally pure Ni, replotted from reference [23]. It is observed that the onsets of Ni and Mo oxidation occur at nearly the same potential (≈ -0.25 V_{SCE}) however the dissolution of Mo does not occur until a more positive potential (≈ 0 to 0.1 V_{SCE}) most likely associated with the oxidation of Mo(IV) species to the more soluble Mo(VI) species. This is accompanied by a transition in the polarization curve from a passive plateau to an increasing current – potential curve, characteristic of transpassive behavior. This confirms the hypothesis that the oxides of Mo formed in the potential range of the active to passive transition are not soluble while oxidized Ni is soluble. Thus, we would expect a Ni-Mo alloy to exhibit selective Ni dissolution in this potential domain, leaving behind a residual Mo oxide film. For E > 0 V_{SCE}, Mo dissolution is significantly enhanced.

The potential range in which Mo oxidation occurs without measurable dissolution corresponds well with the domain of the active to passive transition (A1) of the ternary alloy. It is therefore reasonable to attribute the lower critical current measured for the ternary alloy in this domain to the build-up of Mo oxides. These results suggest that Mo oxides formed during active to passive transition facilitates the nucleation and growth of the passive film.

3.4. Passive film formation and dissolution

3.4.1. Spontaneous passivation (potential domain A1)

The growth of the oxide film in the potential domain A1, where the effect of Mo was most significant, was further investigated. The spontaneous passivation of the alloys was monitored as a function of time via a cycle of cathodic activation – open circuit potential, referred to as an SP cycle, shown in Fig. 5a and b for Ni22Cr and Ni22Cr10Mo, respectively. Cathodic activation (CA) was achieved by polarizing the alloy to -0.8 V_{SCE} for 200 s. This resulted in a sharp dissolution peak involving all the alloying elements. The excess dissolution of Cr was indicated for both alloys ($\nu'_{Cr} >> \nu_{Ni}$) and excess Mo for the Ni22Cr10Mo alloy ($\nu'_{Mo} >> \nu_{Ni}$). We refer to this as cathodic activation, as it corresponds to the dissolution of the passive film. Spontaneous passivation was then observed on the release of the potential to E_{oc} (see inset). This is indicated by the excess Ni dissolution ($\nu_{Ni} > \nu'_{Cr}$) observed during this period, and the increase in E_{oc}, which quickly stabilized at ~ -0.2 V_{SCE} for both alloys. Mo accumulation was also indicated for the Ni22Cr10Mo alloy where $\nu_{Ni} > \nu'_{Mo}$.

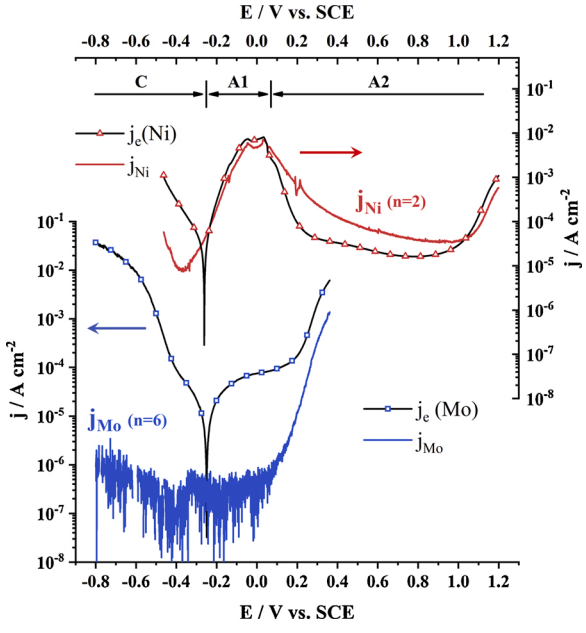

Fig. 4. The elemental resolved polarization curves of pure Ni and Mo in 2 M H_2SO_4. The Ni data are replotted from reference [23].

Spontaneous passivation, Fig. 5, showed not only the accumulation of Cr and Mo in the oxide film, but also indicated the effect of the enriched oxide film on the corrosion rate. For the Ni22Cr alloy, the Ni dissolution rate reached a steady-state value (ν_{Ni} =3 ng cm^{-2} s^{-1}, E_{oc} = -0.24 V_{SCE}) with Cr dissolving congruently ($\nu'_{Cr} = \nu_{Ni}$). This is a factor of 4 lower than the dissolution rate observed for pure Ni under nominally identical conditions [23] (ν_{Ni} =12 ng cm^{-2} s^{-1}, E_{oc} = -0.31 V_{SCE}) and illustrates the effect of Cr on spontaneous passivation. However, this was still a 10-fold increase relative to the open circuit dissolution rate before cathodic activation (ν_{Ni} = 0.3 ng cm^{-2} s^{-1}, E_{oc} = -0.003 V_{SCE}), when the material was protected by the air-formed oxide film. This demonstrates that the air-formed passive film on Ni22Cr was more efficient at lowering the corrosion rate than the film formed spontaneously in H_2SO_4.

For the Ni22Cr10Mo alloy, the spontaneous dissolution rate decreased to nearly the detection limit ($\nu_{Ni} \approx$ 0.4 ng cm^{-2} s^{-1}, E_{oc} = -0.22 V_{SCE}) following spontaneous passivation, comparable to the open circuit dissolution rate before cathodic activation. This demonstrated the effect of Mo on reinforcing spontaneous passivation of Ni22Cr10Mo alloy as compared to the binary alloy.

The surface excess of Cr (Θ_{Cr}) and Mo (Θ_{Mo}) during spontaneous passivation of Ni22Cr10Mo (Fig. 5b) may be calculated according to Eq. 3, assuming Ni completely dissolved into the solution. The calculation yielded $\Theta_{Cr} \approx$ 25 ng cm^{-2} and $\Theta_{Mo} \approx$ 16 ng cm^{-2}, while for the Ni22Cr alloy, $\Theta_{Cr} \approx$ 40 ng cm^{-2}, although the error was large.

3.4.2. Anodic passivation

Passivation at higher potential in the passive domain[2] (A2) was investigated for both alloys by stepping to a more positive potential, E = 0.3 V_{SCE}, (Fig. 1) following the SP cycle. The resulting dissolution profiles for the anodic passivation are shown in Fig. 6a and b for Ni22Cr and Ni22Cr10Mo, respectively. The anodic step occurs at t = 0 as indicated. Prior to this, the alloy was allowed to corrode freely at open circuit. Again, the efficiency of the spontaneously formed passive film on the ternary alloy is indicated by the decreased open circuit dissolution rate for t < 0.

During the anodic potential step, Ni was selectively removed from the surface ($\nu_{Ni} >> \nu'_{Cr}$) for both Ni22Cr and Ni22Cr10Mo alloys. This is consistent with the growth of the Cr-enriched passive film. A Mo dissolution peak was observed for Ni22Cr10Mo which is nearly congruent with Ni dissolution (see below) and may be attributed to the formation of slightly soluble Mo(VI). The following open circuit corrosion rate for t > 200 s was somewhat higher for the binary alloy as compared to the ternary alloy but the difference was less marked than following spontaneous passivation (t < 0). That the post-AP corrosion rate of the ternary alloy was similar to that of the binary alloy is not

[2] We use the term " passive " to refer to the potential domain were the current is relatively independent of potential in the polarization curve. As spontaneous passivation was demonstrated to occur at potentials below the passive domain, the term is used simply as a convention.

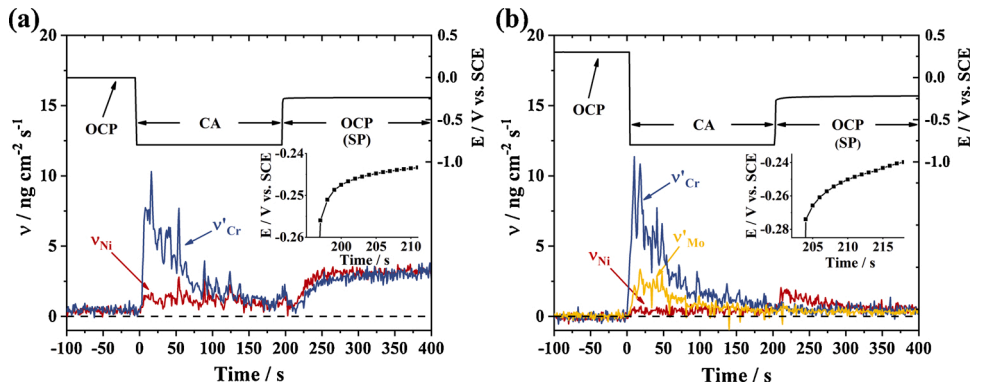

Fig. 5. Normalized elemental dissolution rates (ν'_{Cr} and ν'_{Mo}) recorded during cathodic activation for Ni22Cr (a) and Ni22Cr10Mo (b) in deaerated 2 M H_2SO. Insets show the first 15 s of the open circuit potential after cathodic activation.

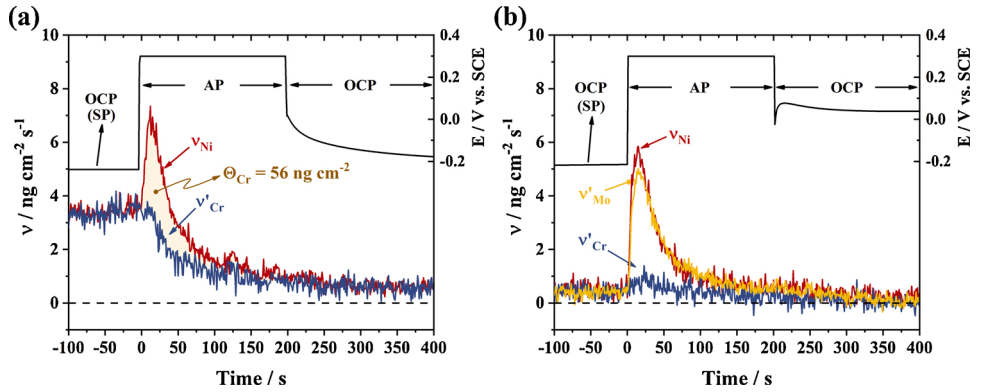

Fig. 6. Normalized elemental dissolution rates (ν'_{Cr} andν'_{Mo}) recorded during anodic passivation (0.3 V_{SCE}) for Ni22Cr (a) and Ni22Cr10Mo (b) in deaerated 2 M H_2SO_4. Surface acumulations were determined by integration and mass balance, exemplified in yellow for Θ_{Cr} in Fig. 6a (For interpretation of the references to colour in this figure legend, the reader is referred to the web version of this article.).

surprising since Cr accumulation occurred simultaneously with Mo dissolution, partially eliminating the Mo-oxides formed during spontaneous passivation.

By mass balance, the surface accumulation of Cr was Θ_{Cr} =56 ng cm^{-2} and Θ_{Cr} =81 ng cm^{-2} for Ni22Cr and Ni22Cr10Mo, respectively, corresponding to estimated film thicknesses of 0.16 nm and 0.23 nm, assuming a uniform Cr_2O_3 layer with the usual density of 5.22 g cm^{-3}. These extremely low values suggest that passivation may not be uniform on the surface and/or the oxides formed are much less dense than the standard densities used in the calculation. Similarly low values have been determined in previous studies for stainless steel [3,36], C-22 Ni alloy [23], and a Ni-based high entropy alloy [37].

The faradaic yield of dissolution during anodic passivation can be determined by comparing the sum of the elemental current, Σj_M, with the convoluted external electrical current, j_e*. This comparison for Ni22Cr and Ni22Cr10Mo is shown in Fig. 7. For the binary alloy, the decreasing background dissolution from the open circuit corrosion (j_{BG}) preceding the polarization was calculated and subtracted [3]. The resulting difference between Σj_M and j_{BG} was compared with j_e*, and a faradaic yield of 80 % was obtained. The quantity of excess charge calculated by integrating $j_\Delta = j_e^* - \Sigma j_M - j_{BG}$ was 450 μC cm^{-2}, corresponding to an estimated uniform Cr_2O_3 film thickness of ≈ 0.23 nm. Again, the low value suggests that the film is not uniform but the good agreement between the coulometric analysis and the elemental mass

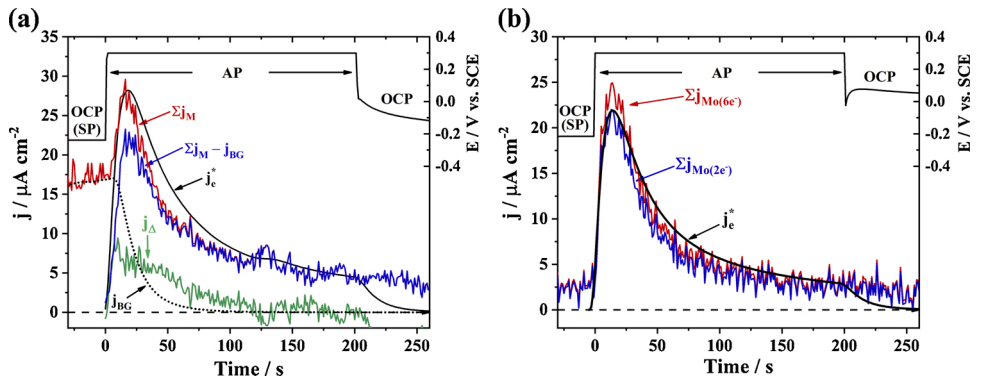

Fig. 7. Comparison of the convoluted electrical current, j_e*, and the sum of the elemental currents, Σj_M, for (a) Ni22Cr and (b) Ni22Cr10Mo alloys. Mo($6e^-$) and Mo ($2e^-$) indicate the number of electrons contributed by Mo is chosen as 6 and 2 respectively.

balance indicates the quantitative nature of the approach.

The faradaic yield of dissolution for Ni22Cr10Mo is shown in Fig. 7b. Two separate curves are shown in which n = 2 (lower) and n = 6 (upper) were assumed for Mo dissolution, as there is some ambiguity as to the precise dissolution reaction, Mo(IV) → Mo(VI) or Mo(0) → Mo(VI). In either case, with only 10 % Mo, the assumption of the Mo oxidation state did not significantly affect the calculated faradaic yield which was near 100 %. The quantity of excess charge, Θ_e, was obtained by integrating the difference, $j_\Delta = j_e^* - \Sigma j_{Mo(2e^-)}$. The value of $\Theta_e = 269$ μC cm^{-2}, similar in magnitude to the value obtained by mass balance. This result confirms the hypothesis that the oxidation of Mo in the high potential domain results in a predominately soluble form of Mo oxide.

3.4.3. Potentiostatic cycles

The interplay between the different elements may be apprehended by their behavior over several active-passive cycles. The surface excess of Cr and Mo, Θ_{Cr} and Θ_{Mo}, were determined as a function of time during a sequence of activation-passivation cycles as shown in Fig. 8. The cycles consisted of cathodic activation (200 s at E = -0.8 V_{SCE}), OCP (300 s), anodic passivation (200 s at E = 0.3 V_{SCE}), and OCP (300 s) referred to as an AP cycle. For both alloys, the formation of the passive film was demonstrated by the increase of Θ_{Cr} during spontaneous passivation and more significantly during anodic passivation. The removal of the passive film was detected by the rapid decrease of Θ_{Cr} during cathodic activation. The cycles demonstrate that the passive film was formed and removed, however, the slow increase in the background may suggest some non-reversibility in the process and/or changes in the near-surface alloy composition. The Mo surface excess, Θ_{Mo}, for the Ni22Cr10Mo alloy showed a similar trend, increasing during spontaneous passivation, decreasing slightly during anodic passivation, and decreasing during cathodic activation. Overall, the results indicate that, for AP cycles, passivation and activation were reasonably reversible within experimental error.

The reversibility of spontaneous passivation during repeated SP cycles was investigated for Ni22Cr10Mo in Fig. 9, where the surface excess of Cr and Mo, Θ_{Cr} and Θ_{Mo} during four SP cycles are shown. The accumulation and subsequent dissolution of surface Cr oxide was clear in the variation of Θ_{Cr} with time, however, Θ_{Mo} increased steadily, indicating that Mo enriched more in the spontaneous passivation (SP) period than was removed during the cathodic activation period, resulting in a net increase in Mo accumulation with every cycle. The maximum amount of Cr decreased with successive cycles such that by the fourth cycle Cr accumulation and dissolution were considerably attenuated. This result

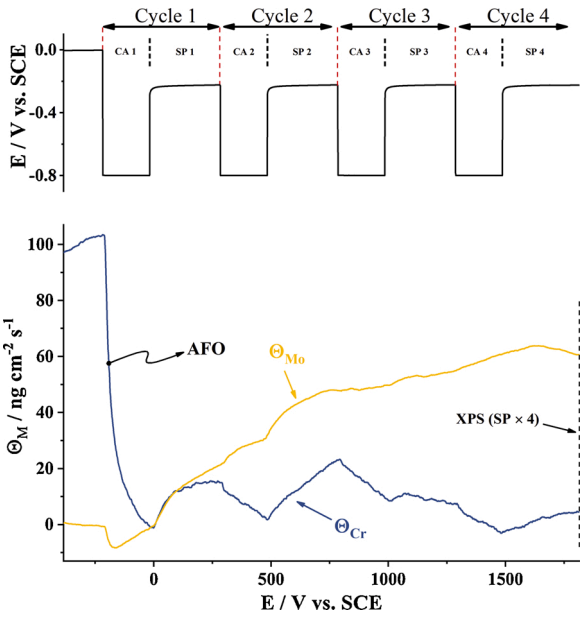

Fig. 9. The surface excess of Cr (Θ_{Cr}) and Mo (Θ_{Mo}) during SP cycles for Ni22Cr10Mo in deaerated 2 M H_2SO_4. The upper part of the figure shows the corresponding potential. AFO: air-formed oxide.

suggests a cumulative action of the Mo build-up: as the Mo content of the surface was enhanced during successive SP cycles, the formation of Cr oxide was hindered.

These results for both Cr and Mo are very similar to previous results for alloy C-22, a commercial Ni-Cr-Mo alloy [23]. The maximum accumulation of Cr throughout the AP cycles, Θ_{Cr}(max), was approximately 114 ng cm^{-2}, similar to that of the C-22 alloy, Θ_{Cr}(max) =133 ng cm^{-2}. During spontaneous passivation, Θ_{Cr} from the first spontaneous passivation was around 15 ng cm^{-2}, similar to that of the commercial alloy.

3.5. XPS characterization

To gain further insight into the chemical nature of Cr and Mo in the oxide film, as observed by AESEC, XPS was performed at various stages in the cyclic experiments. To avoid atmospheric contamination, the electrochemical experiments were performed in an inert atmosphere

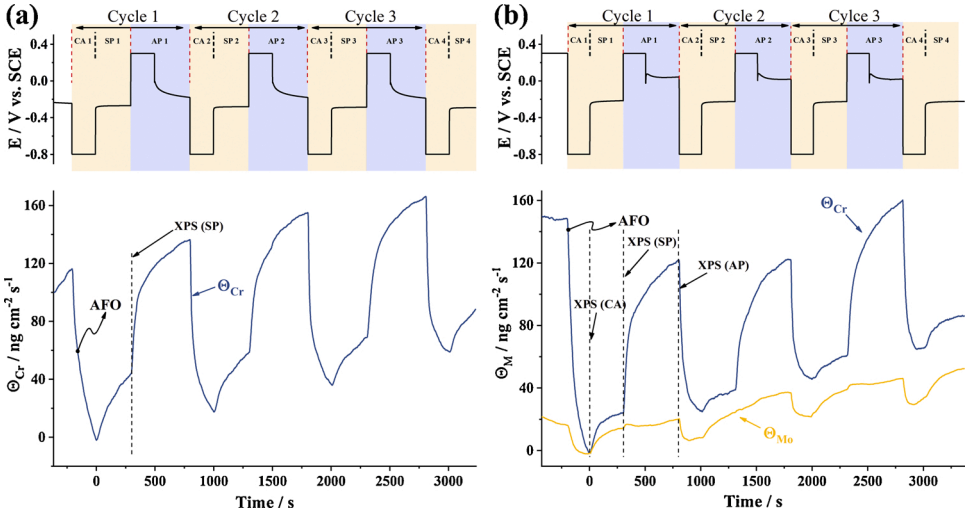

Fig. 8. The surface excess of Cr (and Mo) for Ni22Cr (a) and Ni22Cr10Mo (b) during AP cycles in deaerated 2 M H_2SO_4. The upper part of the figure shows the corresponding potential. The activation cycle with spontaneous passivation is highlighted in light yellow, the anodic passivation in light blue. AFO: air-formed oxide (For interpretation of the references to colour in this figure legend, the reader is referred to the web version of this article.).

glovebox and the specimens transferred into the XPS vacuum system without exposure to the ambient atmosphere. The parameters for deconvoluting the high-resolution spectra were described in the experimental section. The fitting of the Mo 3d signal for samples exposed to H_2SO_4 required the consideration of sulfate and sulfide signals, due to the overlap of S 2 s and Mo 3d bands. The presence of sulfate and sulfide was confirmed by the S 2p band in the survey spectrum, and their ratio was obtained from the high-resolution spectrum of the S 2p region (neither shown here). The ratio of different Mo species was then calculated after subtracting the contribution of sulfate and sulfide signals (S 2 s).

XPS results for the air-formed oxide on Ni22Cr10Mo alloy are given in Fig. 10 and may be considered a reference for the electrochemical experiments. For Ni and Mo, the metallic peak dominated the spectra. Small quantities of Mo and Ni oxide were detected with 8% NiO and 14 % $Ni(OH)_2$ and 15 % Mo(IV) and 20 %Mo(VI). The Cr spectrum showed oxide as the predominate species, with Cr(III) oxide and hydroxide accounting for 25 % and 28 % respectively with no detectable Cr(VI).

XPS spectra obtained after different steps of a single anodic passivation (AP) cycle for Ni22Cr10Mo are shown in Fig. 11. The spectra represent the surfaces obtained after cathodic activation (CA), spontaneous passivation (SP), and anodic passivation (AP) as indicated in Fig. 8. Fig. 12 shows the spectra obtained after four cycles of spontaneous passivation (SP) as indicated in Fig. 9. The relative intensities of the integrated peaks for the different species of each element for each phase of the cycles are presented in Fig. 13.

Cathodic activation (Fig. 11a) led to an increase in the fraction of Cr (0) (76 %) as compared to the same material with air-formed oxides (48 %), consistent with the partial removal of the passive film by cathodic activation. The Ni(0) and Mo(0) showed only a slight increase (9% and 3%, respectively). This is consistent with the intense Cr dissolution peaks observed in Fig. 5b. It should be noted that even under the nitrogen atmosphere in the glove box, it is impossible to obtain spectra of the surface immediately after cathodic activation, as the surface is exposed to the electrolyte for several seconds, and some degree of reoxidation most certainly occurs during this period.

Spontaneous passivation occurred during the open circuit exposure following the cathodic activation. The corresponding XPS spectra are shown in Fig. 11b. A decrease of ~10 % was observed in Ni(0), Cr(0) and Mo(0) fractions and an increase of the respective oxidized species, as shown in Fig. 12. The passivating effect of this film on the corrosion rate was indicated in Fig. 5b where the elemental dissolution rates were reduced to around the detection limit after film formation.

Anodic passivation was investigated in Fig. 11c after a single complete AP cycle. The ratio of Cr(III)/Cr(0) was further enhanced, consistent with the AESEC results shown in Fig. 6b. The relative amount of Mo (VI) increased while that of Mo(IV) decreased. These trends are also indicated in Fig. 12. This implies that the passive potential (0.3 V_{SCE}) favored the formation of Mo(VI), in agreement with thermodynamic considerations [23]. The enhanced Mo dissolution observed in the anodic domain of the polarization curve (Fig. 3) and the anodic passivation (Fig. 6b) can, therefore, be attributed to the formation of Mo (VI) in the passive domain which, in an acid solution, is more soluble than the Mo(IV) species.

The accumulation of Mo was observed to increase with successive SP cycles in the AESEC profiles of Fig. 9. To confirm this result and identify the oxidations states of Mo present in the passive film, XPS spectra (Fig. 12) were obtained after a series of four SP cycles. The Mo(0) contribution decreased by nearly 50 % while Cr(0) actually increased slightly by 6% (Fig. 12). These results are qualitatively consistent with the AESEC results of Fig. 9.

The total elemental analysis was determined by combining the elemental analysis from the survey with the oxidation state analysis from the high-resolution spectra. The total composition is shown in Fig. 14a which includes the metallic species. As previously mentioned, the M(0) oxidation states will decrease in percentage as the oxide film thickens because the metallic substrate is masked by the oxide film. These results demonstrate that the oxide film increased in thickness CA < SP < AP as we would expect. The SPx4 was intermediate between CA and SP.

The relative composition of the surface oxides, Fig. 14b, was determined by removing the metallic states from the analysis and normalizing to 100 %. CA and SP have similar composition, although the results of Fig. 14a indicate that the passive film thickness had increased following SP. Although cathodic activation should remove much of the passive film, some degree of spontaneous passivation may happen, due to the inevitable contact with the electrolyte before the sample was taken out of the flow cell, resulting in the re-formation of the oxide. The spontaneously passivated film showed a Cr/Mo oxide ratio of 1.5. This value increased to 4.2 following anodic passivation. Again, this result demonstrates the significant accumulation of Cr during anodic passivation. The ratio of Mo(IV)/Mo(VI) increased from 1.0 (SP) to 2.1 (AP) with a slight appearance of Mo(V) species. A series of four SP cycles led to a marked enhancement of Mo (Mo/Cr = 1.3) and a Mo(VI)/Mo(IV) ratio = 0.36.

There is consistency between the XPS results (Fig. 14) and the surface excess profiles from AESEC (Figs. 8b and 9). The ratio of Mo/Cr in the surface oxides following spontaneous passivation was determined to be 1.2 by XPS compared with 1.4 by AESEC. After anodic passivation, this ratio decreased to 0.4 for XPS and 0.2 for AESEC. The results were less consistent after four SP cycles with a Mo/Cr ratio of 2.4 for XPS as compared to 12 for AESEC although the trend of Mo accumulating on the surface was consistent in both experiments.

The origin of the discrepancies in quantification between XPS and AESEC is difficult to assess, however the local nature of XPS analysis compared to the global nature of AESEC may play a role. For XPS, only a small surface area (0.028 mm^2) in the center of the dissolution crater is measured while AESEC gives an average value over the entire working electrode area. Add to this the fact that the active-passive cycle experiment may be difficult to reproduce after several cycles, a problem which is further exacerbated due to the transfer protocol to XPS.

The Ni22Cr10Mo alloy showed a significantly lower spontaneous dissolution rate after open circuit passivation than did the Ni22Cr alloy. To gain insight into the origin of this difference, the spontaneously

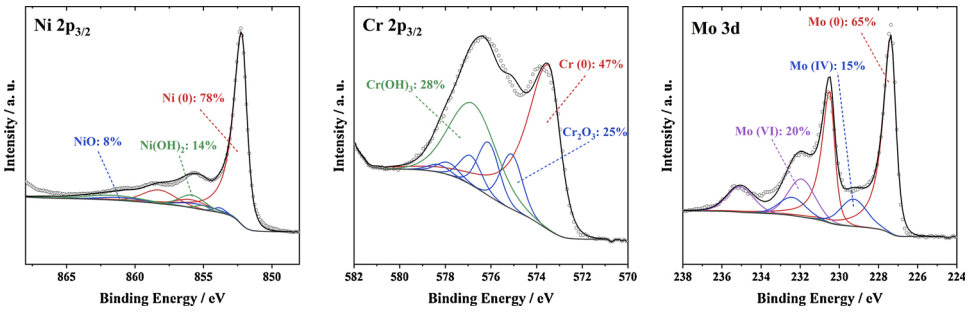

Fig. 10. Deconvoluted XPS high-resolution spectrum of Ni($2p_{3/2}$), Cr($2p_{3/2}$), and Mo(3d) regions recorded for the air-formed oxide on Ni22Cr10Mo alloy.

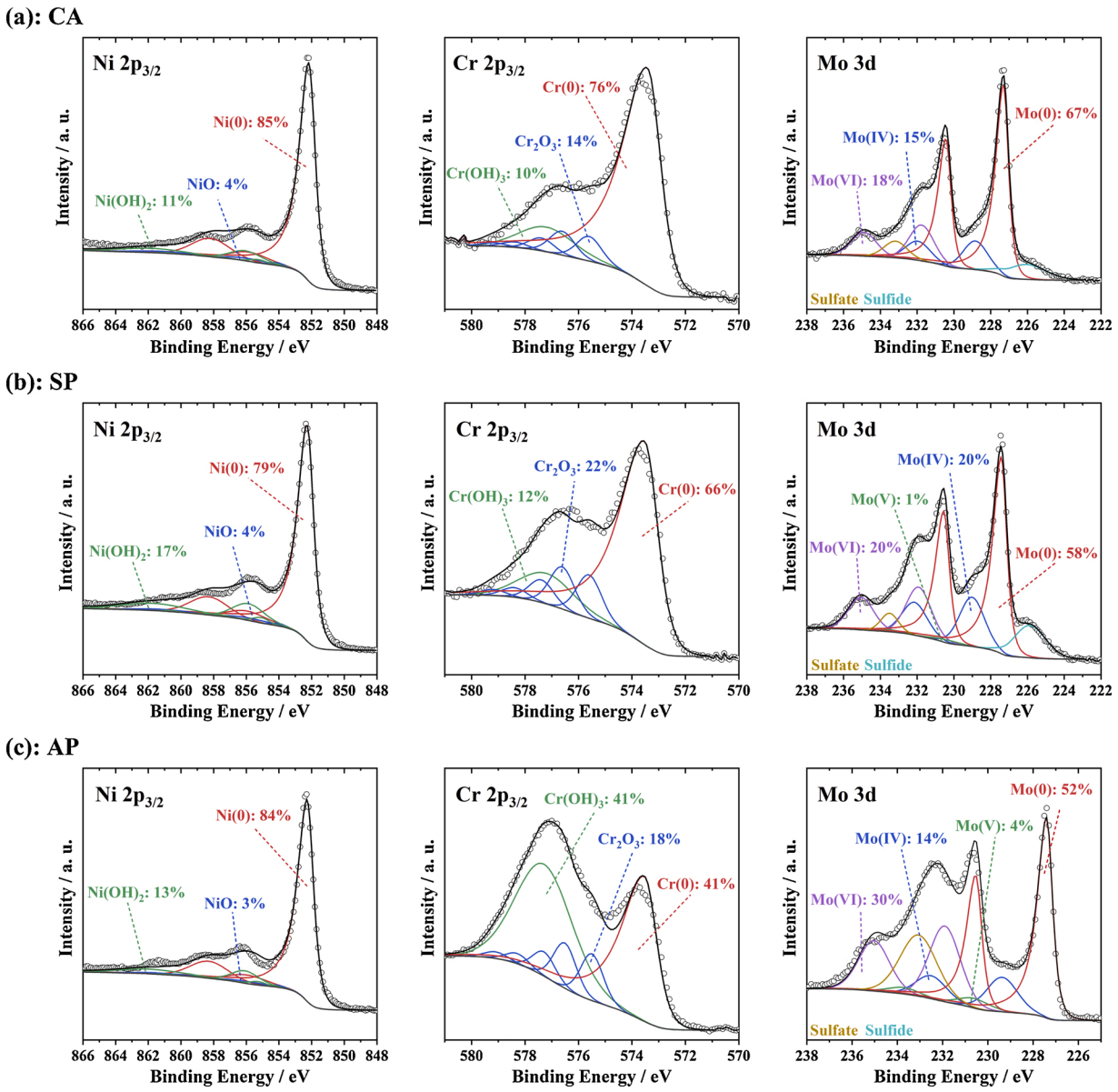

Fig. 11. Deconvoluted XPS high-resolution spectrum of Ni($2p_{3/2}$), Cr($2p_{3/2}$), and Mo(3d) recorded at various steps within the AP cycle. (a): cathodic activation. (b): spontaneous passivation. (c): anodic passivation.

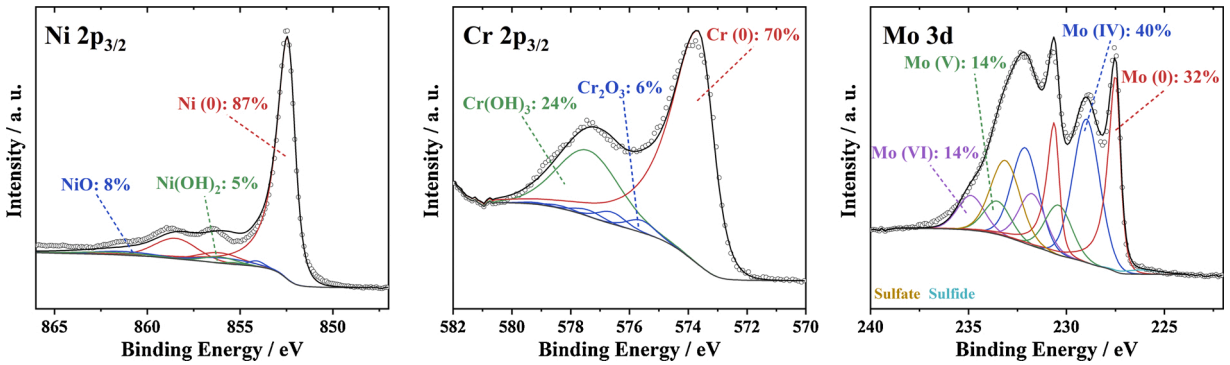

Fig. 12. Deconvoluted XPS high-resolution spectrum of Ni($2p_{3/2}$), Cr($2p_{3/2}$) and Mo(3d) recorded after a sequence of four SP cycles.

formed passive film on Ni22Cr was also analyzed by XPS, as shown in Fig. 15. The sample was cathodically activated and then released to OCP for 300 s. Both NiO and Cr_2O_3 fitting parameters were included in the deconvolution; however, they were not required to model the experimental spectra, suggesting the absence of these species at the surface. Instead, both spectra were dominated by signals of the metallic state,

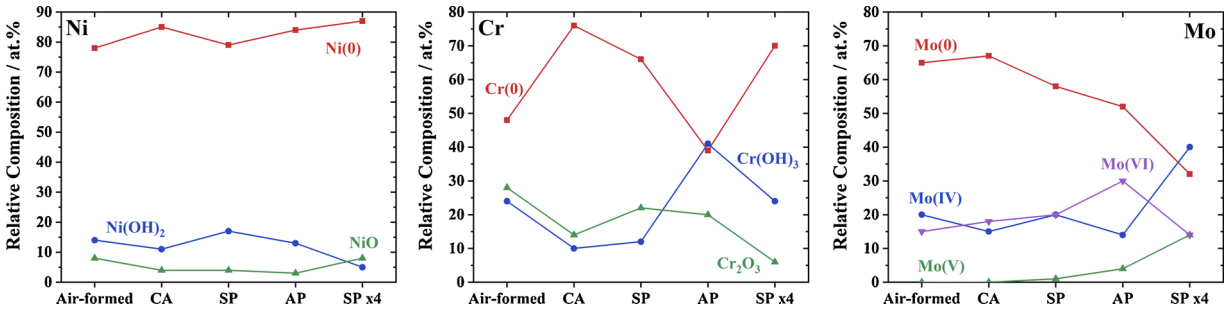

Fig. 13. Comparison of relative composition for Ni, Cr, and Mo species obtained at various stages of the experiment cycle.

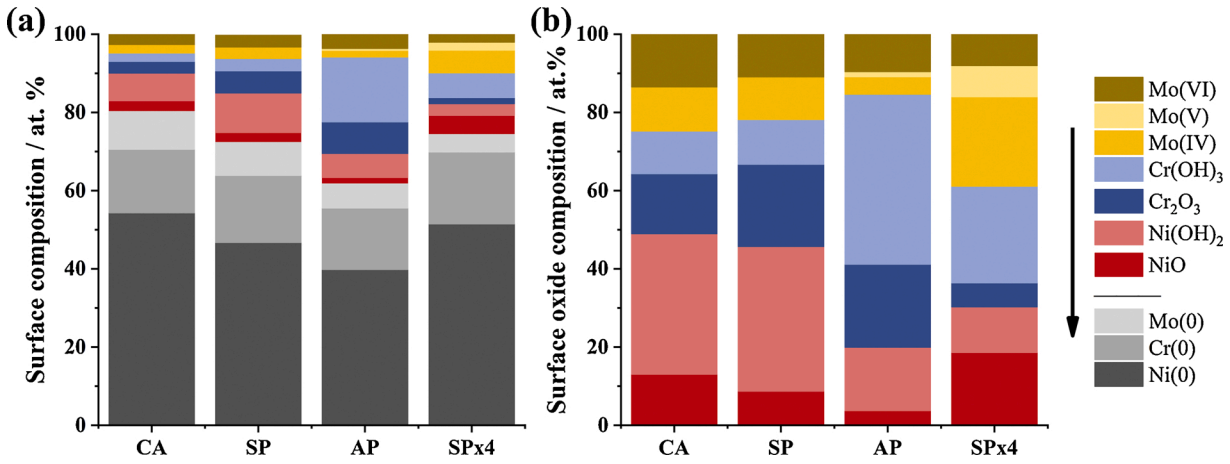

Fig. 14. (a) Total XPS elemental analysis including the zero oxidation state elements and (b) Normalized surface composition of the oxides on Ni22Cr10Mo following CA, SP, AP, and SP x4 (fractions given in at.%). The species are arranged in the legend in the same order (indicated by the arrow) as on the graph.

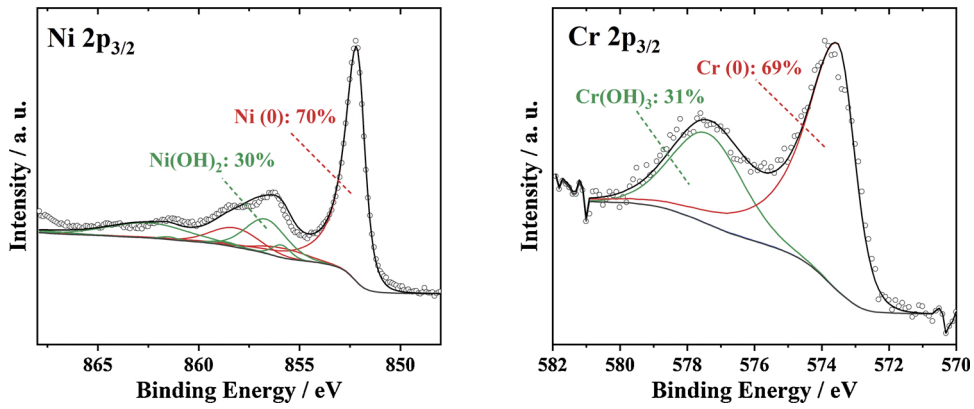

Fig. 15. Spontaneous passivation: Deconvoluted XPS high-resolution spectra of Ni($2p_{3/2}$) and Cr($2p_{3/2}$) from the Ni22Cr alloy after a CA-OCP cycle.

with small amounts of hydrated oxides (i.e. $Ni(OH)_2$ and $Cr(OH)_3$). Taking the AESEC results into account, we can attribute the enriched Cr observed during spontaneous passivation to the formation of $Cr(OH)_3$. This is in contrast to the Ni22Cr10Mo alloy where the Cr 2p spectra showed a $Cr_2O_3/Cr(OH)_3$ ratio of 1.8 (Fig. 11).

These results suggest that Mo oxides formed in the A1 potential domain facilitate the oxidation of Cr to Cr_2O_3 rather than $Cr(OH)_3$ which may be considered a step in the nucleation of the passive film as a high $Cr_2O_3/Cr(OH)_3$ ratio has been associated with a more protective oxide, at least for one alloy C2000 (Ni23Cr16Mo1.6Cu) [4].

4. Discussion

For the majority of Cr containing alloys (Fe-Cr, Ni-Cr), Cr is the major element enriched in the passive film. This occurs via a mechanism of selective dissolution of Ni or Fe, leaving behind a residual Cr(III) oxide/hydroxide film, i.e.

$$2Ni_xCr + 3H_2O \rightarrow 2xNi^{2+}(aq) + Cr_2O_3(s) + 6H^+ + (6+4x)e^- \quad (8)$$

$$Ni_xCr + 3H_2O \rightarrow xNi^{2+}(aq) + Cr(OH)_3(s) + 3H^+ + (3+2x)e^- \quad (9)$$

It is well known that in sulfuric acid, the critical current for passivation decreases markedly with increasing %Cr, as less Ni dissolution is necessary to produce an equivalent Cr(III) film [38].

How are these reactions affected by Mo alloying? In the experimental

conditions of this work, it appears that Mo will affect the film when passivation occurs at low potentials (A1) because, unlike Ni and Cr, Mo oxidation yields completely insoluble oxidation products in this potential domain. Therefore Mo(IV)-oxides build-up on the surface. This Mo oxide accumulation apparently promotes Eq. 8 over Eq. 9 thereby enhancing the ratio of $Cr_2O_3/Cr(OH)_3$ resulting in a film with improved barrier properties.

As the potential increases, the excess Mo will dissolve such that the high potential passive film shows a similar composition and corrosion resistance properties for both alloys. The spontaneously formed passive film probably does not correspond to the stable film formed at longer times and/or higher potential which has been the object of most ex situ spectroscopic studies to date. More likely it represents a "pre-passive" film [39] that may be considered as an unstable film during the early stages of growth.

The low-potential accumulation of Mo during spontaneous passivation was previously attributed to the oxidation of Mo(0) to MoO_2 (Eq. 10) in the low potential domain, based on thermodynamic considerations [23]. Its subsequent dissolution at higher potential was attributed to the oxidation of Mo and partial oxidation of preformed MoO_2 to MoO_4^{2-}, Eq. 11. In acid solution, molybdate exists in equilibrium with precipitated molybdates, indicated as $MoO_3{\cdot}H_2O$(s) (Eq. 12), which would explain the partial dissolution of Mo observed at high potential. The solid molybdate species may also be linked to the series of polymeric species such as $Mo_7O_{24}^{6-}$ and $Mo_8O_{26}^{4-}$ known to form under these conditions [40].

$$Mo + 2H_2O \rightarrow MoO_2 + 4H^+ + 4e^- \quad (10)$$

$$MoO_2 + 2H_2O \rightarrow MoO_3{\cdot}H_2O\ (s) + 2H^+ + 2e^- \quad (11)$$

$$MoO_3{\cdot}H_2O\ (s) \rightarrow MoO_4^{2-} + 2H^+ \quad (12)$$

The dissolution of molybdic acid (Eq. 12) is known to be slow and the kinetics and mechanism of this reaction have been investigated in sulfuric acid in the framework of Mo extraction from ores [41].

Alloys containing Mo have frequently been associated with an enhanced self-healing ability of the passive film [9,31]. A defect in the passive film results in the underlying alloy being exposed to the electrolyte, followed by the re-formation of the passive film. The formation of a defect is to some extent simulated in this paper by the removal of the passive film by cathodic activation, and its subsequent re-formation initiated by the spontaneous passivation. Similar ideas have been proposed previously [42]. Newman [43] investigated repassivation of Fe-19Cr and Fe-19Cr-2.5Mo (wt.%) in 1 M HCl using a scratching electrode device. During repassivation, Mo significantly inhibited dissolution after the removal of 1–2 atom layers of Fe-Cr alloy. Thus, he concluded that Mo took effect at a sub-monolayer level, e.g. the Mo accumulated at kink or step sites. Scanning tunneling microscopy results given by Maurice et al. [9] suggest that, for an austenitic stainless steel single crystal surface in 0.05 M H_2SO_4, Mo nanostructures would form selectively in local defects in the passive film. In this work, the accumulation of Mo measured from mass balance during spontaneous passivation yielded an extremely low value (16 ng cm^{-2}, less than a monolayer), which would suggest that Mo was not homogeneously distributed but enriched at local sites.

Spontaneous passivation was also observed for the binary Ni22Cr alloy; however, the spontaneously formed passive film on Ni22Cr was less efficient than the film formed on Ni22Cr10Mo under identical conditions. The XPS results suggested that the formation of Mo(IV)-oxides on the surface favored the formation of Cr_2O_3 during spontaneous passivation. Recent publications have suggested similar effects. A first-principles investigation by Samin et al. [44] showed that the addition of Mo to the alloy stabilized oxygen adsorption, thus making the oxide more favorable. Yu et al. [45] reported that the addition of 6 wt.% Mo inhibited Kirkendall void formation by promoting the nucleation of a metastable $Ni_{2-x}Cr_xO_3$ corundum structure.

There have been some discussions recently regarding the role of $NiCr_2O_3$ in the passivation of Ni-Cr and Ni-Cr-Mo alloys [22]. In the data presented here, the mass balance calculations assume that oxidized Ni is nearly 100 % soluble. Therefore, it is impossible to detect the formation of Ni oxide independent of the other alloying components. The near 100 % faradaic efficiency for anodic passivation (Fig. 7) suggests that it makes a very small contribution at best. At higher pH however, Ni (II)-oxides are much less soluble than in 2 M H_2SO_4, and very different results might be expected [22].

The relatively complex chemistry of Mo and its transitory existence in the passive film may explain some of the disagreement in the literature concerning its presence and nature in the passive film. It has been reported for stainless steels in HCl solutions that during active dissolution, the oxidation state of Mo was Mo(IV) according to Olefjord et al. [10,46]; however, it was Mo(VI) according to Hashimoto et al. [13]. Our results would support the Mo(IV) theory, though both oxidation states were present after spontaneous passivation. Passivation at 0.3 V_{SCE} resulted in the increase of Mo(VI) (the thermodynamically predominant oxidation state of Mo [24] at 0.3 V_{SCE}) and the decrease of Mo(IV). To our knowledge, there are no data in the literature concerning Ni22Cr10Mo alloys in this electrolyte to confirm this attribution. In acidic chloride solution, Olefjord et al. [10] also reported that Mo was significantly enriched as Mo(VI) in the passive film in a Mo-alloyed austenitic stainless steel during anodic passivation.

The effect of Mo for anodic passivation was less obvious in this work, however the low pH may have masked the effect. Local breakdown of the passive film in Cl^- containing solutions may be due in part to the recombination of metal cation vacancies, e.g. V''_{Ni} and V'''_{Cr}, expressed in the conventional Kröger-Vink notation [45,47,48]. It has been proposed that doping Ni and Cr oxides with Mo(VI) may create defects in the film by replacing Ni or Cr in the oxide lattice (e.g. $Mo^{4\cdot}_{Ni}$ and $Mo^{3\cdot}_{Cr}$) thereby eliminating the metal cation vacancies and thereby hindering local film breakdown.

These results confirm the mechanisms proposed in the previous AESEC study of commercial alloy C-22, which also contained Fe (3.7 wt. %), W (2.8 wt.%), and Mn (0.3 wt.%). The critical and passive current densities were quasi-identical in this work and the previous study, indicating that the other alloying elements did not play a significant role in the passivation mechanisms. Therefore, we may generalize the results obtained with a ternary Ni-Cr-Mo alloy to similar commercial systems.

5. Conclusions

The electrochemical behavior of Ni22Cr and Ni22Cr10Mo alloys and pure Mo were investigated by elemental resolved polarization curves in aerated and deaerated sulfuric acid solutions. Alloying with Mo improved the active to passive transition probably by favoring the nucleation and growth of Cr_2O_3 with respect to $Cr(OH)_3$ by a factor of 10 less decrease in the critical current density. This was associated with a significant Mo accumulation. In the passive domain, the current density was not significantly different between the two alloys suggesting that the passive film formed in the high potential domain ($E > 0$ V_{SCE}) was independent of Mo.

These results were consistent with the electrochemistry of pure Mo which oxidized to form insoluble Mo oxides in the low potential domain (A1, $E < \sim 0$ V_{SCE}) but formed soluble Mo species at higher potential. A similar behavior was observed for Mo in the alloys with preferential Ni and Cr dissolution in the low potential domain and the accumulation oxidized Mo in the oxide film.

The accumulation of Cr (on Ni22Cr) or Cr and Mo (on Ni22Cr10Mo) were observed in real-time during spontaneous passivation in the low potential domain ($E \approx$ -0.2 V_{SCE}) under free corrosion conditions. The Mo enriched passive film formed on the ternary alloy showed a markedly reduced free corrosion rate as compared to the binary alloy and a higher $Cr_2O_3/Cr(OH)_3$ ratio. It is reasonable to infer that the Mo enrichment in this potential domain favors the nucleation and growth of

Cr_2O_3 thereby improving the corrosion resistance of the film. Repeated spontaneous passivation – cathodic activation cycles showed a continuous accumulation of Mo in the oxide and a decrease in the quantity of Cr.

Anodic passivation resulted in a further increase of Cr on the surfaces of both Ni22Cr and Ni22Cr10Mo. However, Mo dissolved nearly congruently with Ni at this step for the ternary alloy and the resulting passive film was depleted in Mo as compared to the film formed spontaneously at lower potential. The ratio of Mo(VI)/Mo(IV) increased demonstrating that Mo dissolution was due to the formation of partly soluble Mo(VI) species.

CRediT authorship contribution statement

Xuejie Li: Conceptualization, Methodology, Investigation, Writing - original draft. **Jeffrey D. Henderson:** Conceptualization, Methodology, Investigation, Writing - review & editing. **Fraser P. Filice:** Conceptualization, Methodology, Writing - review & editing (XPS). **Dmitrij Zagidulin:** Conceptualization, Methodology (XPS). **Mark C. Biesinger:** Methodology, Validation, Writing - review & editing (XPS). **Fan Sun:** Conceptualization, Writing - review & editing (alloy synthesis). **Bingnan Qian:** Conceptualization, Investigation (alloy synthesis). **David W. Shoesmith:** Conceptualization, Writing - review & editing, Supervision. **James J. Noël:** Conceptualization, Writing - Review & Editing, Supervision. **Kevin Ogle:** Conceptualization, Writing - review & editing, Final Editing, Supervision.

Declaration of Competing Interest

The authors report no declarations of interest.

Acknowledgments

Author X.L. would like to acknowledge the Chinese Scholarship Council (CSC) for financial support. Author J.D.H. is grateful to be the recipient of an Alexander Graham Bell Canada Graduate Scholarship (NSERC). Author J.D.H. also acknowledges the financial support of the ECS H. H. Uhlig Summer Fellowship.

Appendix A. Supplementary data

Supplementary material related to this article can be found, in the online version, at doi:https://doi.org/10.1016/j.corsci.2020.109015.

References

[1] R.M. Carranza, M.A. Rodríguez, Crevice corrosion of nickel-based alloys considered as engineering barriers of geological repositories, NPJ Mater. Degrad. 1 (2017).
[2] S. Boudin, J.L. Vignes, G. Lorang, M. Da Cunha Belo, G. Blondiaux, S.M. Mikhailov, J.P. Jacobs, H.H. Brongersma, Analytical and electrochemical study of passive films formed on nickel—chromium alloys: influence of the chromium bulk concentration, Surf. Interface Anal. 22 (1994) 462–466.
[3] K. Ogle, M. Mokaddem, P. Volovitch, Atomic emission spectroelectrochemistry applied to dealloying phenomena II. Selective dissolution of iron and chromium during active–passive cycles of an austenitic stainless steel, Electrochim. Acta 55 (2010) 913–921.
[4] X. Zhang, D. Zagidulin, D.W. Shoesmith, Characterization of film properties on the NiCrMo alloy C-2000, Electrochim. Acta 89 (2013) 814–822.
[5] G.O. Ilevbare, G.T. Burstein, The role of alloyed molybdenum in the inhibition of pitting corrosion in stainless steels, Corros. Sci. 43 (2001) 485–513.
[6] N.S. Zadorozne, C.M. Giordano, M.A. Rodríguez, R.M. Carranza, R.B. Rebak, Crevice corrosion kinetics of nickel alloys bearing chromium and molybdenum, Electrochim. Acta 76 (2012) 94–101.
[7] F. Bocher, R. Huang, J.R. Scully, Prediction of critical crevice potentials for Ni-Cr-Mo alloys in simulated crevice solutions as a function of molybdenum content, Corrosion 66 (2010), 055002-055002-055015.
[8] K. Lutton Cwalina, C.R. Demarest, A.Y. Gerard, J.R. Scully, Revisiting the effects of molybdenum and tungsten alloying on corrosion behavior of nickel-chromium alloys in aqueous corrosion, Curr. Opin. Solid State Mater. Sci. (2019).
[9] V. Maurice, H. Peng, L.H. Klein, A. Seyeux, S. Zanna, P. Marcus, Effects of molybdenum on the composition and nanoscale morphology of passivated austenitic stainless steel surfaces, Faraday Discuss. 180 (2015) 151–170.
[10] I. Olefjord, B.-O. Elfstrom, The composition of the surface during passivation of stainless steels, Corrosion 38 (1982) 46–52.
[11] D. Zagidulin, X. Zhang, J. Zhou, J.J. Noël, D.W. Shoesmith, Characterization of surface composition on Alloy 22 in neutral chloride solutions, Surf. Interface Anal. 45 (2013) 1014–1019.
[12] J.R. Cahoon, R. Bandy, Auger electron spectroscopic studies on oxide films of some austenitic stainless steels, Corrosion 38 (1982) 299–305.
[13] K. Hashimoto, K. Asami, K. Teramoto, An X-ray photo-electron spectroscopic study on the role of molybdenum in increasing the corrosion resistance of ferritic stainless steels in HC1, Corros. Sci. 19 (1979) 3–14.
[14] A.E. Yaniv, The composition of passive films on ferritic stainless steels, J. Electrochem. Soc. 124 (1977).
[15] H. Ogawa, H. Omata, I. Itoh, H. Okada, Auger electron spectroscopic and electrochemical analysis of the effect of alloying elements on the passivation behavior of stainless steels, Corrosion 34 (1978) 52–60.
[16] K. Gusieva, K.L. Cwalina, W.H. Blades, G. Ramalingam, J.H. Perepezko, P. Reinke, J.R. Scully, Repassivation behavior of individual grain facets on dilute Ni–Cr and Ni–Cr–Mo alloys in acidified chloride solution, J. Phys. Chem. C 122 (2018) 19499–19513.
[17] N. Ebrahimi, M.C. Biesinger, D.W. Shoesmith, J.J. Noël, The influence of chromium and molybdenum on the repassivation of nickel-chromium-molybdenum alloys in saline solutions, Surf. Interface Anal. 49 (2017) 1359–1365.
[18] M. Sakashita, N. Sato, The effect of molybdate anion on the ion-selectivity of hydrous ferric oxide films in chloride solutions, Corros. Sci. 17 (1977) 473–486.
[19] A.C. Lloyd, J.J. Noël, S. McIntyre, D.W. Shoesmith, Cr, Mo and W alloying additions in Ni and their effect on passivity, Electrochim. Acta 49 (2004) 3015–3027.
[20] B. Zhang, X.X. Wei, B. Wu, J. Wang, X.H. Shao, L.X. Yang, S.J. Zheng, Y.T. Zhou, Q. Q. Jin, E.E. Oguzie, X.L. Ma, Chloride attack on the passive film of duplex alloy, Corros. Sci. 154 (2019) 123–128.
[21] H. Habazaki, A. Kawashima, K. Asami, K. Hashimoto, The corrosion behavior of amorphous Fe-Cr-Mo-P-C and Fe-Cr-W-P-C alloys in 6 M HCl solution, Corros. Sci. 33 (1992) 225–236.
[22] K.L. Cwalina, H.M. Ha, N. Ott, P. Reinke, N. Birbilis, J.R. Scully, In operando analysis of passive film growth on Ni-Cr and Ni-Cr-Mo alloys in chloride solutions, J. Electrochem. Soc. 166 (2019) C3241–C3253.
[23] X. Li, K. Ogle, The passivation of Ni-Cr-Mo alloys: time resolved enrichment and dissolution of Cr and Mo during passive-active cycles, J. Electrochem. Soc. 166 (2019) C3179–C3185.
[24] K. Ogle, Atomic emission spectroelectrochemistry: real-time rate measurements of dissolution, corrosion, and passivation, Corrosion 75 (2019) 1398–1419.
[25] V. Shkirskiy, P. Maciel, J. Deconinck, K. Ogle, On the time resolution of the atomic emission spectroelectrochemistry method, J. Electrochem. Soc. 163 (2015) C37–C44.
[26] K. Ogle, S. Weber, Anodic dissolution of 304 stainless steel using atomic emission spectroelectrochemistry, J. Electrochem. Soc. 147 (2000).
[27] M.C. Biesinger, B.P. Payne, A.P. Grosvenor, L.W.M. Lau, A.R. Gerson, R.S.C. Smart, Resolving surface chemical states in XPS analysis of first row transition metals, oxides and hydroxides: Cr, Mn, Fe, Co and Ni, Appl. Surf. Sci. 257 (2011) 2717–2730.
[28] M.C. Biesinger, B.P. Payne, L.W.M. Lau, A. Gerson, R.S.C. Smart, X-ray photoelectron spectroscopic chemical state quantification of mixed nickel metal, oxide and hydroxide systems, Surf. Interface Anal. 41 (2009) 324–332.
[29] M.C. Biesinger, C. Brown, J.R. Mycroft, R.D. Davidson, N.S. McIntyre, X-ray photoelectron spectroscopy studies of chromium compounds, Surf. Interface Anal. 36 (2004) 1550–1563.
[30] P.A. Spevack, N.S. McIntyre, Thermal reduction of molybdenum trioxide, J. Phys. Chem. 96 (1992) 9029–9035.
[31] J.R. Hayes, J.J. Gray, A.W. Szmodis, C.A. Orme, Influence of chromium and molybdenum on the corrosion of nickel-based alloys, Corrosion 62 (2006) 491–500.
[32] A. Mishra, D. Shoesmith, P. Manning, Materials selection for use in concentrated hydrochloric acid, Corrosion 73 (2016) 68–76.
[33] M. B.Rockel, The effect of molybdenum on the corrosion behavior of iron-chromium alloys, Corrosion 29 (1973) 393–396.
[34] K. Ogle, J. Baeyens, J. Swiatowska, P. Volovitch, Atomic emission spectroelectrochemistry applied to dealloying phenomena: I. The formation and dissolution of residual copper films on stainless steel, Electrochim. Acta 54 (2009) 5163–5170.
[35] K. Lutton, K. Gusieva, N. Ott, N. Birbilis, J.R. Scully, Understanding multi-element alloy passivation in acidic solutions using operando methods, Electrochem. Commun. 80 (2017) 44–47.
[36] B. Laurent, N. Gruet, B. Gwinner, F. Miserque, K. Rousseau, K. Ogle, Dissolution and passivation of a silicon-rich austenitic stainless steel during active-passive cycles in sulfuric and nitric acid, J. Electrochem. Soc. 164 (2017) C892–C900.
[37] X. Li, J. Han, P. Lu, J.E. Saal, G.B. Olson, G.S. Frankel, J.R. Scully, K. Ogle, Communication—dissolution and passivation of a Ni-Cr-Fe-Ru-Mo-W high entropy alloy by elementally resolved electrochemistry, J. Electrochem. Soc. 167 (2020).
[38] J.R. Myers, F.H. Beck, M.G. Fontana, Anodic polarization behavior of nickel-chromium alloys in sulfuric acid solutions, Corrosion 21 (1965) 277–287.
[39] R. Kirchheim, Kinetics of film formation on Fe-Cr alloys, in: P. Marcus, B. Baroux, M. Keddam (Eds.), European Symposium on Modifications of Passive Films, The Institute of Materials, Paris, France,, 1993, pp. 102–107.
[40] P. Jakupi, F. Wang, J.J. Noël, D.W. Shoesmith, Corrosion product analysis on crevice corroded Alloy-22 specimens, Corros. Sci. 53 (2011) 1670–1679.

[41] E.Y. Nevskaya, I.G. Gorichev, A.D. Izotov, B.E. Zaitsev, K.M. Al'dieva, A. M. Kutepov, Kinetics of molybdenum(VI) oxide dissolution in sulfuric acid solutions, Theor. Found. Chem. Eng. 38 (2004) 316–321.
[42] J.D. Henderson, N. Ebrahimi, X. Li, K. Ogle, J.J. Noel, The complementarity of Cr and Mo in reinforcing oxide protectiveness on Ni-Cr-Mo alloys, in: 236th ECS Meeting (October 13-17, 2019), ECS, 2019.
[43] R.C. Newman, The dissolution and passivation kinetics of stainless alloys containing molybdenum—1. Coulometric studies of Fe□Cr and Fe□Cr□Mo alloys, Corros. Sci. 25 (1985) 331–339.
[44] A.J. Samin, C.D. Taylor, First-principles investigation of surface properties and adsorption of oxygen on Ni-22Cr and the role of molybdenum, Corros. Sci. 134 (2018) 103–111.
[45] X.-x. Yu, A. Gulec, C.M. Andolina, E.J. Zeitchick, K. Gusieva, J.C. Yang, J.R. Scully, J.H. Perepezko, L.D. Marks, In situ observations of early stage oxidation of Ni-Cr and Ni-Cr-Mo alloys, Corrosion 74 (2018) 939–946.
[46] I. Olefjord, Surface composition of stainless steels during anodic dissolution and passivation studied by ESCA, J. Electrochem. Soc. 132 (1985).
[47] X.X. Yu, A. Gulec, Q. Sherman, K.L. Cwalina, J.R. Scully, J.H. Perepezko, P. W. Voorhees, L.D. Marks, Nonequilibrium solute capture in passivating oxide films, Phys. Rev. Lett. 121 (2018), 145701.
[48] M. Urquidi, Solute-vacancy interaction model and the effect of minor alloying elements on the initiation of pitting corrosion, J. Electrochem. Soc. 132 (1985).